electronics

Article

Modeling Thermal Impedance of IGBT Devices Based on Fractional Calculus Techniques

Nan Yang [1], Zhikui Yang [2,*], Yaoling Huang [1], Wen Yang [1], Wei Liu [1] and Xi Chen [2,*]

[1] State Grid Hubei Direct Current Company, No. 6 Changliu Road, Yichang 443002, China; yangn51@hb.sgcc.com.cn (N.Y.); huangyl23@hb.sgcc.com.cn (Y.H.); yangw83@hb.sgcc.com.cn (W.Y.); liuwei42@hb.sgcc.com.cn (W.L.)

[2] College of Electrical Engineering and New Energy, China Three Gorges University, No. 8 Daxue Road, Yichang 443002, China

* Correspondence: ctguzk@ctgu.edu.cn (Z.Y.); eene_chenxi@ctgu.edu.cn (X.C.)

Abstract: The thermal impedance characteristics of insulated gate bipolar transistor (IGBT) modules are critical for the thermal management and design of electronic devices. This paper proposes a fractional-order equivalent thermal impedance model, which is inspired by the correlation between multi-time-scale dissipation characteristics of heat conduction processes and fractional calculus. The fractional-order equivalent thermal impedance model is derived based on the connection between fractional-order calculus and the Foster thermal network model in mathematical operations, with only two parameters to be identified: heat capacity C and fractional order α. Moreover, this paper provides a parameter identification method for the proposed fractional-order equivalent thermal impedance model based on the multi-objective particle swarm optimization (MOPSO) algorithm. In order to validate the effectiveness and superiority of this work, experiments and comparative works are provided in this paper. The results indicate that the fractional-order equivalent thermal impedance model can accurately describe the frequency domain characteristic curves of the thermal impedance of the Foster thermal network model for IGBT modules, with the difference between the amplitude frequency characteristics not exceeding 1 dB and the difference between the phase frequency characteristics not exceeding 1° within the operating frequency range of (1 kHz, 1 MHz).

Keywords: IGBT modules; thermal impedance model; fractional-order; parameter identification

check for updates

Citation: Yang, N.; Yang, Z.; Huang, Y.; Yang, W.; Liu, W.; Chen, X. Modeling Thermal Impedance of IGBT Devices Based on Fractional Calculus Techniques. *Electronics* **2024**, *13*, 4423. https://doi.org/10.3390/electronics13224423

Academic Editor: Francesco Giuseppe Della Corte

Received: 7 October 2024
Revised: 6 November 2024
Accepted: 8 November 2024
Published: 12 November 2024

Copyright: © 2024 by the authors. Licensee MDPI, Basel, Switzerland. This article is an open access article distributed under the terms and conditions of the Creative Commons Attribution (CC BY) license (https://creativecommons.org/licenses/by/4.0/).

1. Introduction

With the rapid development of power electronics technology, efficient and reliable power conversion and control have become indispensable in modern power conversion systems [1–3]. IGBT devices, which combine the metal-oxide semiconductor field-effect transistor's advantages of high input impedance and high switching speed with the bipolar junction transistor's advantage of high conductivity characteristics, basically play the electronic switch role in various power conversion systems [4,5]. Their application includes but is not limited to renewable energy systems, electric vehicles, rail transportation, household appliances, industrial motor control, aerospace, etc. [6–11]. With recent improvements, the performance of IGBTs has significantly advanced, specifically in terms of smaller chip size, lower power losses, and faster switching speed, while the voltage ratings and current capacities of IGBTs have also been gradually increasing [12–15]. However, with the lifting of processing voltage and current levels, the devices are subjected to increasingly high thermal stresses, which pose challenges to their lifespan and reliability [16–19].

Basically, thermal resistance and heat capacity are two fundamental parameters that describe the thermal characteristics of IGBT modules, and their combination forms the thermal impedance model of IGBT modules, which is crucial for ensuring the reliability and performance of IGBT modules. Currently, a vast variety of thermal impedance models for IGBT modules have been proposed, with the Cauer thermal network model and the

Foster thermal network model being the more commonly used ones [20–23]. By correlating each layer within the IGBT device with a pair of parameters in the Cauer thermal network model, a Cauer thermal network model can be constructed, which can be used to simulate the internal heat conduction process of IGBT devices [24,25]. However, measuring the heat transfer in each layer of the device during operation is quite challenging. The Foster thermal network model can also provide a simple yet effective means of analyzing the device's thermal characteristics, but it does not directly correspond to the physical structure of each layer of the device [26,27]. Therefore, obtaining the parameters of the Foster thermal network model is relatively straightforward. In practice, both the Cauer and Foster thermal network models use multiple parameters to describe the thermal impedance characteristics of IGBT modules. However, an excessive number of parameters can increase the complexity of the model and make it more difficult to identify the model parameters. Therefore, it is necessary to find a more concise and intuitive way to characterize the thermal impedance characteristics of IGBTs.

In theory, the heating and heat conduction process of IGBT devices is a kind of dissipation process with a memory effect. Specifically, during the operation of IGBT devices or modules, electrical energy is converted into thermal energy, which tends to be transferred from high-temperature areas to low-temperature areas, that is, from the inside of the device to the surrounding environment, until reaching a thermal equilibrium state [28–30]. Generally, the devices have a certain thermal inertia, which means that there is still a certain amount of heat inside the device after the power is turned off. This heat does not immediately disappear but gradually dissipates through thermal conduction and other means. Accordingly, the accumulation or disappearance of heat is manifested as a dissipation process with typical memory characteristics during the dynamic heat transfer process, i.e., the current temperature distribution depends on the previous temperature state.

Due to the presence of numerous fractional–dimensional phenomena in nature and engineering, fractional calculus has been widely used in science and engineering, especially in the description of complex and nonlinear systems [31,32]. Fractional calculus, which generalizes the concepts of differentiation and integration to non-integer orders, has been found to be particularly useful in modeling the behavior of systems with memory effects [33–36]. Therefore, this paper introduces the concept of the fractional-order thermal impedance model and establishes a specific fractional-order equivalent thermal impedance model for describing the thermal impedance characteristics of IGBT modules. Further, this paper introduces a parameter identification method for the fractional-order equivalent thermal impedance models based on the MOPSO algorithm [37,38].

In order to present the detailed modeling and parameter identification processes, the remaining parts of this paper are as follows: Section 2 introduces the modeling and parameter extraction of the Foster thermal network model. Section 3 proposes a fractional-order equivalent thermal impedance model and a model parameter identification method based on the MOPSO algorithm. Section 4 provides experimental verification. Section 5 summarizes the paper.

2. Modeling and Parameter Extraction of the Foster Thermal Network Model

As shown in Figure 1, the junction-to-case structure of the IGBT module is composed of multiple layers. When heat is generated in the IGBT chip, there is a transfer of heat process among different layers due to the presence of temperature differences.

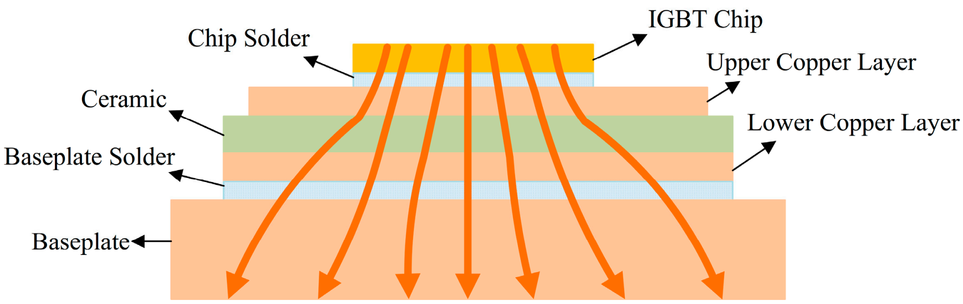

Figure 1. Internal heat transfer diagram of IGBT modules.

Assuming a heating power is applied to the IGBT module, according to the thermoelectric analogy method [39], the heating power can be analogized to the current in an electrical circuit, the temperature difference can be analogized to the voltage difference, the thermal resistance can be analogized to the electrical resistance, and the heat capacity can be analogized to the electrical capacitance. This enables the use of a thermal network model to analyze thermal behavior. The junction temperature calculation formula of IGBT modules is shown in Equation (1):

$$T_j(t_i) = Z_{thjc}(t_i)P + T_c(t_i) \tag{1}$$

Based on Equation (1), the calculation formula of the junction–case thermal impedance of IGBT modules can be obtained as follows:

$$Z_{thjc}(t_i) = \frac{T_j(t_i) - T_c(t_i)}{P} \tag{2}$$

where $T_j(t_i)$ is the junction temperature of IGBT modules at moment t_i, $T_c(t_i)$ is the case temperature of IGBT modules at moment t_i, and P is the heating power of IGBT modules.

The traditional integer-order one-cell Foster thermal network model is shown in Figure 2.

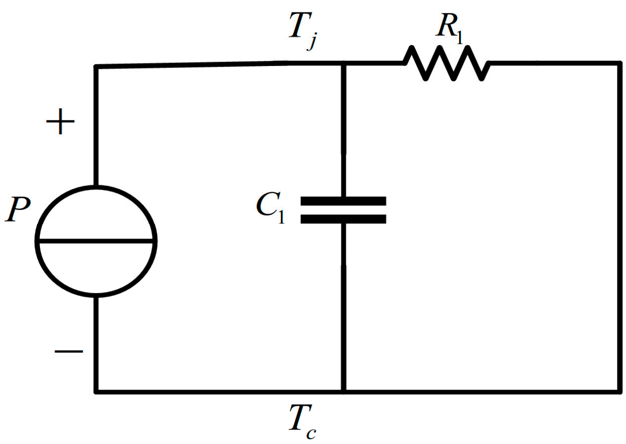

Figure 2. Foster thermal network model with one *R*-*C* cell.

Based on the thermoelectric analogy method, the *s*-domain transfer function expression of the traditional integer-order one-cell Foster thermal network model can be obtained:

$$Z_{thF_1}(s) = \frac{R_1 \cdot \frac{1}{sC_1}}{R_1 + \frac{1}{sC_1}} = \frac{R_1}{1 + sR_1C_1} = \frac{R_1}{1 + s\tau_1} \tag{3}$$

where τ_1 is the time constant, that is, $\tau_1 = R_1C_1$; the term R_1 is the thermal resistance value; the term C_1 is the heat capacity value; and the term s is the complex frequency.

In thermal analysis, the complex frequency s can be used to describe the thermal response of the system. The thermal response equation of the thermal model can be converted to an s-domain equation by the Laplace transform. Let $s = j\omega$, which is the Fourier transform and allows for the thermal impedance model to represent the thermal impedance response of the IGBT module in the frequency domain so that the thermal characteristics of IGBTs in the frequency domain can be effectively studied by the thermal impedance model.

The inverse Laplace transform of Equation (3) can obtain the time domain expression of the thermal impedance response of the integer-order one-cell Foster thermal network model:

$$Z_{thF_1}(t) = R_1(1 - e^{\frac{-t}{\tau_1}}) \tag{4}$$

where the term t is time.

As shown in Figure 3, the integer-order n-cell Foster thermal network model is composed of n-cell heat capacity and thermal resistance parallel structures in series. The corresponding thermal impedance response equation of the integer-order n-cell Foster thermal network model can be expressed as:

$$Z_{thF_n}(t) = \sum_{i=1}^{n} R_i(1 - e^{\frac{-t}{\tau_i}}) \tag{5}$$

where τ_i is the time constant of order i, $\tau_i = R_iC_i$, R_i is the thermal resistance value of order i, and C_i is the heat capacity value of order i. n is the order of the thermal network model and i is a positive integer.

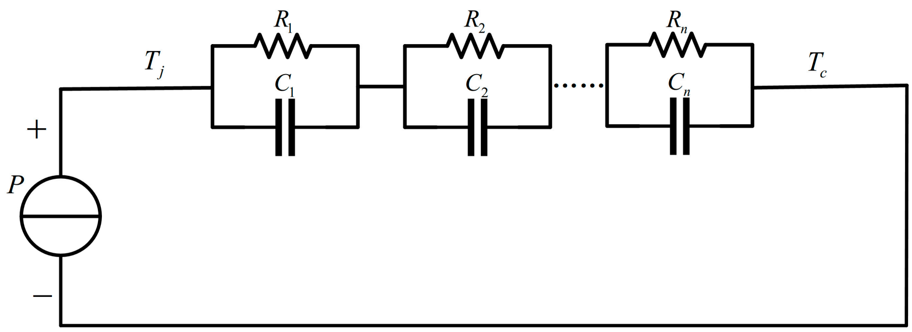

Figure 3. Integer-order n-cell Foster thermal network model.

The thermal resistance and heat capacity parameters in the Foster thermal network model can be obtained by fitting the thermal impedance curve. From Equation (5), it can be seen that the thermal impedance response is a sum of n-order expressions. The higher the order, the more accurate the fitting result, but the fitting process and subsequent handling become more complex. Therefore, considering all factors, an integer-order four-cell Foster thermal network model can be established to fit the thermal impedance curve and obtain the model parameters, with its thermal impedance response equation expressed as:

$$Z_{thF_4}(t) = \sum_{i=1}^{4} R_i(1 - e^{\frac{-t}{\tau_i}}) \tag{6}$$

The parameter extraction flowchart for the Foster thermal network model is shown in Figure 4.

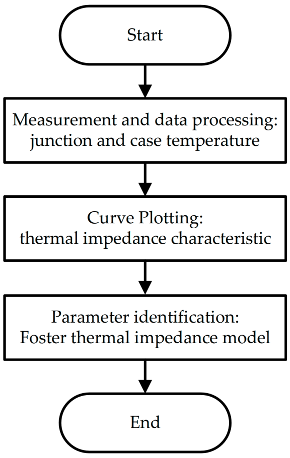

Figure 4. Parameter extraction flowchart for the Foster thermal impedance model.

3. Modeling and Parameter Identification of Fractional-Order Equivalent Thermal Impedance Model

3.1. Modeling Principle and Framework

Based on the analysis of heat transfer within IGBT modules and considering that the Foster thermal network model consists of multiple self-similar structures, a fractional-order equivalent thermal impedance model, as shown in Figure 5, has been established in this paper.

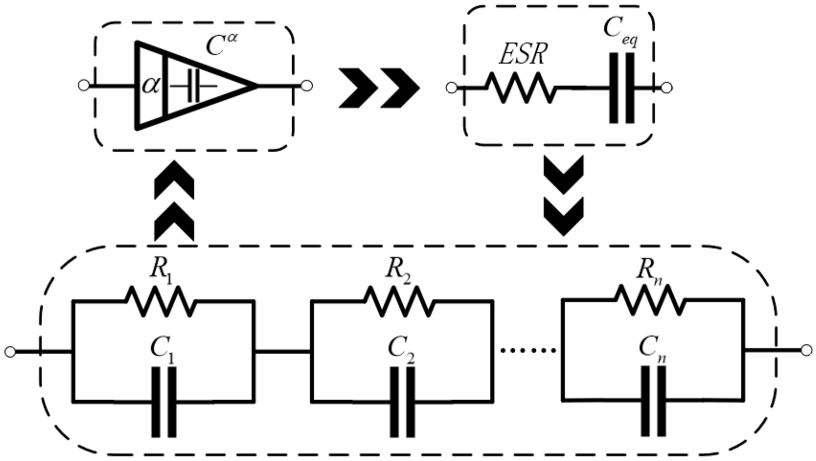

Figure 5. Modeling of fractional-order equivalent thermal impedance model.

The fractional-order equivalent thermal impedance model in Figure 5 represents the nominal value of heat capacity in terms of C. The fractional order α is introduced to correct the heat capacity value C, and $0 < \alpha < 2$. The relationship between the current $i(t)$ and the voltage $u(t)$ of an order-α heat capacity can be governed by:

$$i(t) = C \cdot {}_{0}^{RL}\mathcal{D}_{t}^{\alpha} u(t) \tag{7}$$

Here, α is the order of the capacity. According to Riemann–Liouville definition of fractional calculus, the fractional-order derivative of the heat capacity α is given by:

$${}_{0}^{RL}\mathcal{D}_{t}^{\alpha} f(t) = \frac{1}{\Gamma(n-\alpha)} \frac{d^n}{dt^n} \int_0^t \frac{f(\tau)}{(t-\tau)^{1+\alpha-n}} d\tau \tag{8}$$

Here, $n < \alpha < n+1$, where n is any integer, τ is the variable of integration, and $\Gamma(z)$ is the Gamma function, defined as:

$$\Gamma(z) = \int_0^{\infty} e^{-t} t^{z-1} dt \quad (9)$$

Under the Riemann–Liouville definition, the Laplace transform for the fractional heat capacity can be obtained by:

$$i(s) = \mathcal{L}[i(t)] = C \cdot \mathcal{L}\left[{}_0^{RL}\mathcal{D}_t^{\alpha} u(t)\right] = C \cdot s^{\alpha} U(s) \quad (10)$$

Then one can deduce the s-domain impedance expression for the fractional-order heat capacity:

$$Z_C(s) = \frac{1}{Cs^{\alpha}} \quad (11)$$

The impedance expression is obtained by performing the Fourier transform based on the s-domain transfer function expression of the fractional-order equivalent thermal impedance model:

$$Z_C(j\omega) = \frac{1}{C(j\omega)^{\alpha}} = \frac{cos\frac{\alpha\pi}{2}}{\omega^{\alpha}C} - j\frac{sin\frac{\alpha\pi}{2}}{\omega^{\alpha}C} \quad (12)$$

where j is the complex unit and ω is the frequency.

From Equation (12), it can be seen that the fractional-order equivalent thermal impedance model consists of an equivalent series thermal resistance (ESR) and an equivalent series heat capacity (C_{eq}), with the expressions given by:

$$\begin{cases} ESR = \frac{cos\frac{\alpha\pi}{2}}{\omega^{\alpha}C} \\ C_{eq} = \frac{sin\frac{\alpha\pi}{2}}{\omega^{\alpha}C} \end{cases} \quad (13)$$

According to Equations (12) and (13), it can be seen that by taking different values for the heat capacity C and fractional order α, the different frequency domain characteristic curves of the fractional order equivalent thermal impedance model in the Bode plot can be obtained. Thus, the fractional-order equivalent thermal impedance model can be established based on the frequency domain characteristics of the Foster thermal network model for the IGBT module.

3.2. Parameter Identification Based on the MOPSO Algorithm

One can find that the fractional-order thermal impedance model involves a pair of parameters to be identified [C, α]. To identify the parameter set [C, α] of the fractional-order equivalent thermal impedance model for IGBTs, this paper transforms the problem of identifying parameters into a nonlinear global optimization problem with physical property constraints. Based on the definition of fractional-order heat capacity, the value of order α is restricted to the range $0 < \alpha < 2$. Furthermore, to enhance the accuracy of parameter identification, and considering the range of order α as well as the frequency domain characteristics of the thermal impedance model, the value of heat capacity C is restricted to $0 < C < 100$. Meanwhile, this work utilizes the mean square error (MSE) function as the objective function, where the errors between the frequency domain variation curves of the fractional-order thermal impedance model and the frequency domain characteristic curves of the integer-order n-cell Foster thermal network model are used.

On the one hand, the MSE function $F_1(X)$ of the two models in terms of frequency domain magnitude is:

$$F_1(X) = minMSE = min\sum_{i=1}^{N} \frac{1}{N}\left(\left|Z_{thF_n}(j\omega_i)\right| - |Z_C(j\omega_i)|\right)^2 \quad (14)$$

where $\left|Z_{thF_n}(j\omega_i)\right|$ represents the magnitude of the Foster thermal network model at frequency $\omega = \omega_i$, $|Z_C(j\omega_i)|$ represents the magnitude of the fractional-order equivalent thermal impedance model at frequency $\omega = \omega_i$, ω_i is a positive integer, and N is the total number of data points.

On the other hand, the MSE function $F_2(X)$ of the two models in terms of frequency domain phase is:

$$F_2(X) = minMSE = min\sum_{i=1}^{N} \frac{1}{N}(\angle Z_{thF_n}(j\omega_i) - \angle Z_C(j\omega_i))^2 \tag{15}$$

where $\angle Z_{thF_n}(j\omega_i)$ represents the phase of the Foster thermal network model at frequency $\omega = \omega_i$, and $\angle Z_C(j\omega_i)$ represents the phase of the fractional-order equivalent thermal impedance model at frequency $\omega = \omega_i$.

Accordingly, it is essential to minimize the above two MSE functions simultaneously within the operating frequency band of IGBTs. This is a multi-objective optimization problem. Typically, the sub-objectives of an optimization problem are conflicting—improving one sub-objective may lead to a decrease in the performance of another or several other sub-objectives. That is to say, it is impossible to make several sub-objectives reach the optimal value together at the same time but can only coordinate and compromise among them so that each sub-objective is as much as possible to achieve the best possible optimization. The essential difference with the single-objective optimization problem is that its solution is not unique, but there exists a set of optimal solutions consisting of many Pareto-optimal solutions, and each element in the set is called a Pareto-optimal or a non-dominated optimal solution. Therefore, in this work, the multi-objective particle swarm optimization (MOPSO) is introduced to identify these model parameters [37,38].

The MOPSO algorithm introduces the construction and maintenance of an external archive, which stores non-dominated solutions from each iteration based on dominance relations and eliminates dominated solutions. The specific update process can be expressed as follows:

$$V_i(t+1) = \omega V_i(t) + c_1 r_1 (pBest_i(t) - X_i(t)) + c_2 r_2 (gBest_i(t) - X_i(t)) \tag{16}$$

$$X_i(t+1) = X_i(t) + V_i(t+1) \tag{17}$$

where $X_i(t)$ is the current position of the particle; $V_i(t)$ is the current velocity of the particle; $X_i(t+1)$ is the updated position; $V_i(t+1)$ is the updated velocity; $pBest_i(t)$ represents the local best fitness position, which is the particle's individual historical best position; $gBest_i(t)$ is the global best fitness position, which is the best position in the current particle swarm; ω is the inertia weight factor; c_1 and c_2 are acceleration factors greater than zero; and r_1 and r_2 are random numbers between 0 and 1.

The specific parameter identification process is as follows:

Step 1: Initialize the population and external archive.
Step 2: Calculate the fitness of particles (objective function).
Step 3: Calculate local optimal particles: for local optimal particles, when multiple non-dominated particles are present, one is randomly selected as the local optimum.
Step 4: Select the globally optimal particle: For globally optimal particles, the MOPSO algorithm uses a grid method to determine multiple non-dominated particle global leaders that guide the flight direction of the particle swarm. The grid method divides the range of values of the objective function into grids and determines the leader based on the sparseness of the particles in a single grid; the more particles there are in the grid, the lower the probability of the particles being selected, and therefore, the probability of the particles being selected is higher in a sparser grid.
Step 5: Update the position and velocity of the particle and update the external archive.
Step 6: Determine whether the iteration stop condition is met or not.
Step 7: Output the model parameters when the iteration stop condition is fulfilled.

Figure 6 gives the parameter identification flowchart for the fractional-order equivalent thermal impedance model based on the MOPSO algorithm.

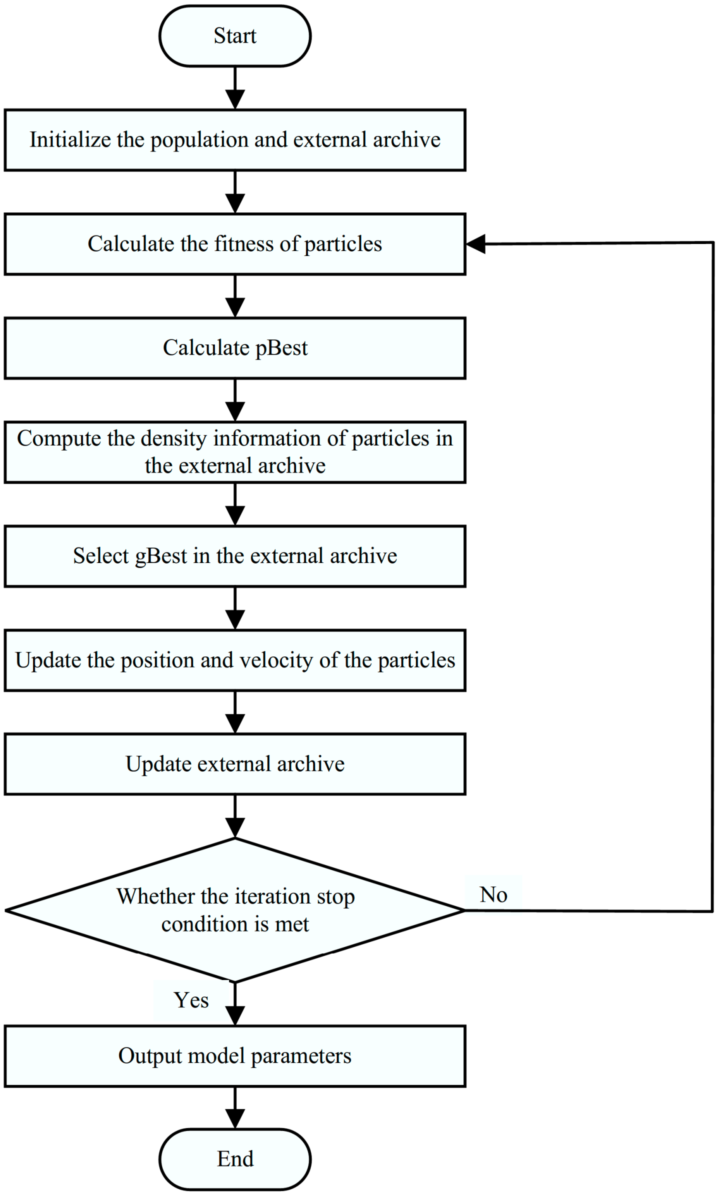

Figure 6. Parameter identification flowchart based on the MOPSO algorithm.

4. Experimental Verification

In order to validate the effectiveness of the proposed fractional-order equivalent impedance model, thermal test scenarios are built up. In this work, this paper used Infineon type-FF75R12RT4 IGBT modules for tests, and in experiments, a programmable DC current source is used to provide a constant heating current of 50 A to the device under test (DUT). Under stable working conditions, the equivalent heating power is approximately 158.5 W. Two K-type thermocouples are used to measure the junction temperature T_j and case temperature T_c of the DUT. The data obtained are collected by a multi-channel temperature tester. The experimental scene is shown in Figure 7.

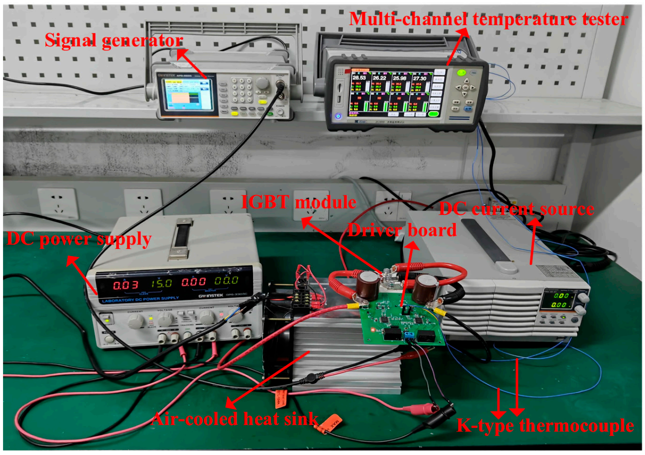

Figure 7. Schematic diagram of the experimental platform.

The measured junction temperature T_j and case temperature T_c of the DUT are shown in Figure 8a. Then, the junction–case thermal impedance Z_{thjc} curve of the DUT can be calculated according to Equation (2), as shown in Figure 8b.

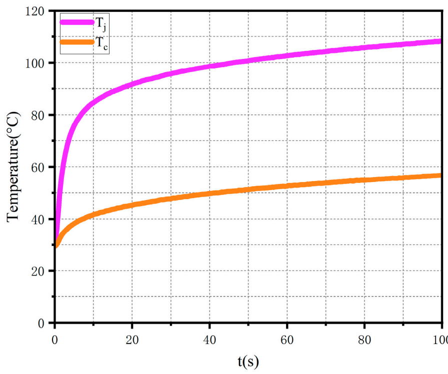

(**a**)

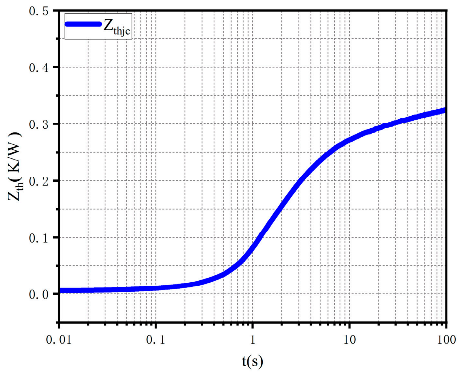

(**b**)

Figure 8. Measurements and calculating results: (**a**) curve graph of junction temperature and case temperature of the IGBT module; (**b**) junction–case thermal impedance curve graph of the IGBT module.

According to the parameter extraction method of the Foster thermal network model described in Section 2, the thermal impedance curve of the IGBT module in Figure 8b is fitted using Equation (6) to extract the parameters of each order in the integer-order four-cell Foster thermal network model. Table 1 shows the results of the extracted parameters for each order of the integer-order four-cell Foster thermal network model. The parameters of the Foster thermal network model for each order are obtained by directly fitting the thermal impedance curve of the DUT using Equation (6). Thus, the parameters in Table 1 are only calculated values.

Table 1. Parameters of integer-order four-cell Foster thermal network model.

i	1	2	3	4
R_i	0.12257	0.12263	0.04616	0.05319
τ_i	2.27168	2.22447	115.99978	14.57902

According to Section 2, the s-domain transfer function expression for an integer-order n-cell Foster thermal network model can be derived as follows:

$$Z_{thF_n}(s) = \sum_{i=1}^{n} \frac{R_i \cdot \frac{1}{sC_i}}{R_i + \frac{1}{sC_i}} = \sum_{i=1}^{n} \frac{R_i}{1 + sR_iC_i} = \sum_{i=1}^{n} \frac{R_i}{1 + s\tau_i} \tag{18}$$

According to Equation (18), performing the Fourier transform yields the frequency domain expression for the thermal impedance of the integer-order n-cell Foster thermal network model:

$$Z_{thF_n}(j\omega) = \sum_{i=1}^{n} \frac{R_i \cdot \frac{1}{j\omega C_i}}{R_i + \frac{1}{j\omega C_i}} = \sum_{i=1}^{n} \frac{R_i}{1 + j\omega R_iC_i} = \sum_{i=1}^{n} \frac{R_i}{1 + j\omega\tau_i} \tag{19}$$

The frequency domain characteristic curve of the thermal impedance of the Foster thermal network model can be obtained through Equation (19). Figure 9 presents the frequency domain characteristic curve of the integer-order four-cell Foster thermal network model thermal impedance, obtained from Table 1 and Equation (19).

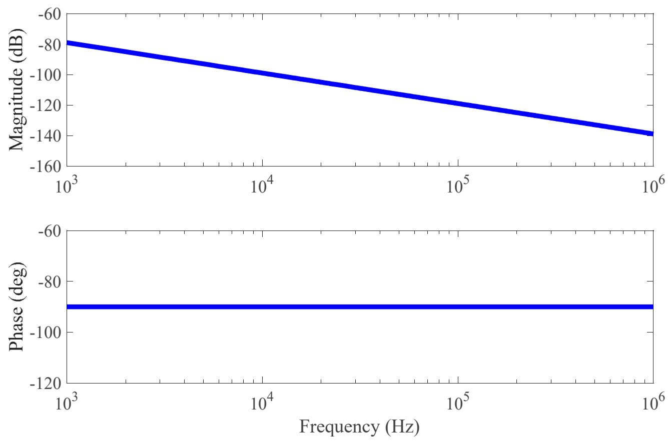

Figure 9. Frequency domain characteristic curves of the thermal impedance of the Foster thermal network model.

The parameter identification of the fractional-order equivalent thermal impedance model is performed according to the parameter identification process based on the MOPSO algorithm proposed in Section 3. According to the number of parameters to be identified in the fractional-order equivalent thermal impedance model, the initial population, 200; the number of iterations, 300; and the number of parameters to be optimized, two, are selected. Data fitting for objective functions (14) and (15) yielded the optimal model parameters $[C, \alpha]$ = [8.97670, 0.99851].

As shown in Figure 10, the variation curves of the amplitude and phase of the thermal impedance of the fractional-order equivalent thermal impedance model are compared with the amplitude frequency and phase frequency characteristic curves of the thermal impedance of the Foster thermal network model of the IGBT module of model Infineon FF75R12RT4. The blue solid line represents the amplitude frequency characteristic and phase frequency characteristic curves of the thermal impedance of the Foster thermal network model of the IGBT module with model number Infineon FF75R12RT4, and the red dotted line represents the variation curves of the amplitude and phase of the thermal impedance of the fractional-order equivalent thermal impedance model. In order to highlight the difference between two different results, Figure 10 is partially enlarged, as shown in Figure 11.

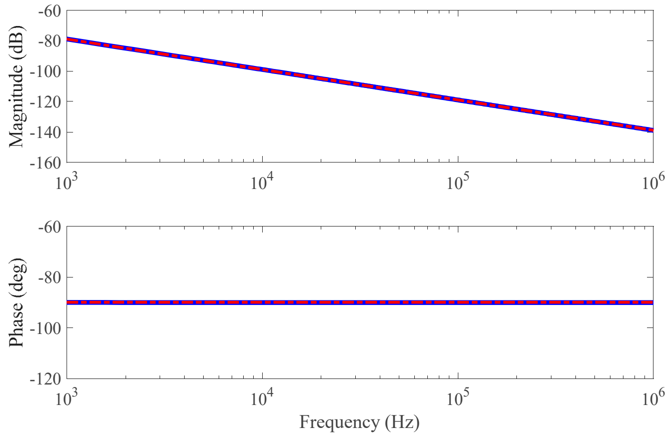

Figure 10. Comparison of frequency domain characteristic curves of thermal impedance between fractional equivalent thermal impedance model and Foster thermal network model.

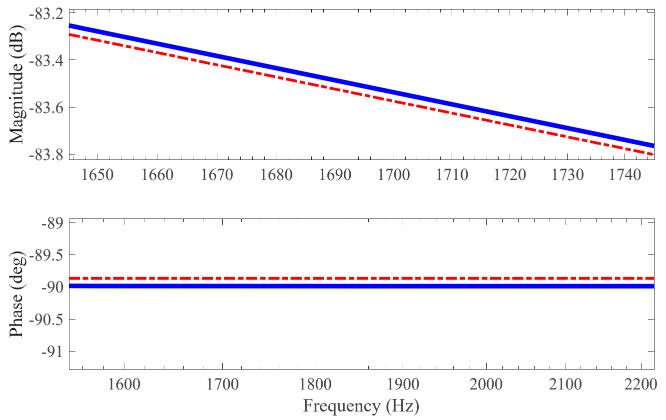

Figure 11. Partially enlarged drawing.

It can be observed that in the frequency range of (1 kHz, 1 MHz), the difference between the amplitude frequency characteristic curves does not exceed 1 dB, and the difference between the phase frequency characteristic curves does not exceed 1°, indicating a high level of precision. This confirms the effectiveness of the fractional-order equivalent thermal impedance model proposed in this paper. In order to highlight the fractional-order equivalent thermal impedance model proposed in this paper, a comparison of the Cauer thermal network model, the Foster thermal network model, and the proposed fractional-order equivalent thermal impedance model is presented in Table 2, focusing on three aspects: modeling accuracy, complexity, and applicable conditions.

Table 2. Model comparison.

Comparative Aspect	Cauer Thermal Network Model	Foster Thermal Network Model	Fractional-Order Equivalent Thermal Impedance Model
Modeling accuracy	High precision at higher orders	High precision at higher orders	Higher accuracy under the same complexity
Complexity	The higher the order, the more complex the model	The higher the order, the more complex the model	Relatively simple
Applicable conditions	Limited application	Widely applied	First proposed but not yet applied

5. Conclusions

This paper studies the Foster thermal network model and its parameter extraction methods. Based on the frequency domain characteristics between the Foster thermal network model and fractional-order elements, a fractional-order equivalent thermal impedance model is proposed, along with a model parameter identification method based on the MOPSO algorithm. Then, this paper extracted the parameters of each order of the integer-order four-cell Foster thermal network model from the thermal impedance characteristic curves of the IGBT module obtained through testing on the experimental platform and plotted the frequency domain characteristic curves of the integer-order four-cell Foster thermal network model. Finally, based on the MOPSO algorithm, the fractional-order equivalent thermal impedance model proposed in this paper was used to perform data fitting of the frequency domain characteristic curves of the Foster thermal network model, thereby validating the proposed fractional-order equivalent thermal impedance model. The results indicate that the fractional-order equivalent thermal impedance model form provided in this paper is more concise compared with the traditional Foster thermal network model and can accurately describe the frequency domain characteristic curves of the thermal impedance of the Foster thermal network model for IGBT modules. It can provide a reference basis for the design and reliability analysis of the circuit system containing these types of elements. Currently, the proposed fractional-order equivalent thermal impedance model is applied in the frequency domain in this paper. In order to further apply the fractional-order equivalent thermal impedance model to the thermal analysis of IGBT devices, it is necessary to transfer the modeling research of fractional-order equivalent thermal impedance to the time domain in the future.

Author Contributions: Conceptualization, X.C.; methodology, Z.Y. and X.C.; software, Z.Y.; validation, Z.Y.; formal analysis, Y.H.; data curation, Z.Y.; writing—original draft preparation, N.Y. and Z.Y.; writing—review and editing, X.C.; visualization, Z.Y.; supervision, W.Y.; project administration, X.C.; funding acquisition, W.L. All authors have read and agreed to the published version of the manuscript.

Funding: This research was funded by Hubei Provincial Natural Science Foundation, China, grant number 2020CFB248 and Research Project of State Grid Hubei Direct Current Company, China, grant number15DQ02-9003001-0507.

Data Availability Statement: Data are contained within the article.

Conflicts of Interest: Authors Nan Yang, Yaoling Huang, Wen Yang and Wei Liu were employed by the company State Grid Hubei Direct Current Company. The remaining authors declare that the research was conducted in the absence of any commercial or financial relationships that could be construed as a potential conflict of interest.

References

1. Wang, J.; Chen, W.; Wu, Y.; Liu, Y.; Wang, T.; Wang, L.; Zhang, J.; Liu, J.; Gan, Y. In Situ Diagnosis for IGBT Chip Failure in Multichip IGBT Modules Based on a Newly Defined Characteristic Parameter Low-Sensitive to Operation Conditions. *IEEE Trans. Power Electron.* **2023**, *38*, 7711–7722. [CrossRef]
2. Lee, H.; Smet, V.; Tummala, R. A Review of SiC Power Module Packaging Technologies: Challenges, Advances, and Emerging Issues. *IEEE J. Emerg. Sel. Top. Power Electron.* **2020**, *8*, 239–255. [CrossRef]
3. Song, Y.; Wang, B. Survey on Reliability of Power Electronic Systems. *IEEE Trans. Power Electron.* **2013**, *28*, 591–604. [CrossRef]
4. Mandeya, R.; Chen, C.; Pickert, V.; Naayagi, R.T.; Ji, B. Gate–Emitter Pre-threshold Voltage as a Health-Sensitive Parameter for IGBT Chip Failure Monitoring in High-Voltage Multichip IGBT Power Modules. *IEEE Trans. Power Electron.* **2019**, *34*, 9158–9169. [CrossRef]
5. Deng, G.; Wang, J.; Wu, Y.; Tan, C.; Liang, S. 3-D Segmented Gate Concept: A New IGBT Solution for Reduced Loss and Improved Safe-Operating Area. *IEEE Trans. Electron Devices* **2023**, *70*, 3172–3178. [CrossRef]
6. Wang, Y.; Wang, J.; Liu, F.; Liu, Q.; Zou, R. An RLL Current Sharing Snubber for Multiple Parallel IGBTs in High Power Applications. *IEEE Trans. Power Electron.* **2022**, *37*, 7555–7560. [CrossRef]
7. Shahsavarian, T.; Zhang, D.; McGinnis, P.; Walker, S.; Zhang, Z.; Cao, Y. Altitude Readiness of High-Voltage IGBTs Subjected to the Partial Discharge at Harsh Environmental Conditions for Hybrid Electric Aircraft Propulsion. *IEEE Trans. Power Electron.* **2022**, *37*, 3733–3736. [CrossRef]
8. Li, T.; Wang, Y.; Zhang, Y.; Fan, J.; Li, X.; Qi, L.; Cui, X. Impacts of the Pressure Distribution on Dynamic Avalanche in Single Press-Pack IGBT Chip. *IEEE Trans. Power Electron.* **2024**, *39*, 8187–8201. [CrossRef]
9. Tu, C.; Xu, H.; Xiao, B.; Lu, J.; Guo, Q.; Long, L. Research on the Influence of Bond Wire Lift-Off Position on the Electro-Thermal Characteristics of IGBT. *IEEE Trans. Electron Devices* **2022**, *69*, 1271–1278. [CrossRef]

10. Xie, D.; Lin, C.; Deng, Q.; Lin, H.; Cai, C.; Basler, T.; Ge, X. Simple Vector Calculation and Constraint-Based Fault-Tolerant Control for a Single-Phase CHBMC. *IEEE Trans. Power Electron.* **2024**, 1–14. [CrossRef]
11. Li, X.; Xu, J.; Chen, Z.; Xu, S.; Liu, K. Real-Time Fault Diagnosis of Pulse Rectifier in Traction System Based on Structural Model. *IEEE Trans. Intell. Transp. Syst.* **2022**, *23*, 2130–2143. [CrossRef]
12. Zhao, Y.; Li, Z.; Zhu, J.; Yang, Y.; Chen, K.; Wang, T.; Xia, Z. A Novel Trench IGBT with N-P-N Polysilicon Gate Structure for Low EMI Noise and High Robustness. *IEEE Trans. Electron Devices* **2024**, *71*, 2508–2516. [CrossRef]
13. Deng, X.; Cheng, Z.; Chen, Z.; Wu, H.; Bai, S.; Li, X.; Li, X.; Chen, W.; Zhang, B. A Hybrid-Channel Injection Enhanced Modulation 4H-SiC IGBT Transistors with Improved Performance. *IEEE Trans. Electron Devices* **2022**, *69*, 4421–4426. [CrossRef]
14. Gu, Y.; Ma, J.; Zhang, L.; Wei, J.; Li, S.; Liu, S.; Zhang, S.; Zhu, J.; Sun, W. Silicon-on-Insulator Lateral Insulated Gate Bipolar Transistor: Current Technologies and Prospects. *IEEE Trans. Electron Devices* **2024**, *71*, 381–392. [CrossRef]
15. Yu, Q.; Huang, J.; Shen, Z.; Zhang, A.; Chen, W. 16kV 4H-SiC Reverse-Conducting IGBT with a Collector-Side Injection-Enhanced Structure for Low Reverse-Conducting Voltage. *IEEE Electron Device Lett.* **2024**, *45*, 1064–1067. [CrossRef]
16. Guo, C.; Cui, S.; Tsai, W.; Liu, Y.; Ding, J.; Li, J.; Chen, Z.; Li, Y.; Pan, S.; Feng, S. Measuring Double-Sided Thermal Resistance of Press-Pack IGBT Modules Based on Ratio of Double-Sided Heat Dissipation. *IEEE Trans. Electron Devices* **2023**, *70*, 1776–1781. [CrossRef]
17. Xu, G.; Shao, L.; Feng, W.; Zhu, W.; Pan, Z.; Li, C.; Zhang, Y.; Xia, L. A Novel IGBT Junction Temperature Detection Based on High-Frequency Model of Inductor Element. *IEEE Trans. Instrum. Meas.* **2023**, *72*, 1500810. [CrossRef]
18. Yang, Y.; Zhang, P. A Novel Converter-Level IGBT Junction Temperature Estimation Method Based on the Bus Voltage Ringing. *IEEE Trans. Power Electron.* **2022**, *37*, 4553–4563. [CrossRef]
19. Jones-Jackson, S.; Rodriguez, R.; Emadi, A. Jet Impingement Cooling in Power Electronics for Electrified Automotive Transportation: Current Status and Future Trends. *IEEE Trans. Power Electron.* **2021**, *36*, 10420–10435. [CrossRef]
20. Bahman, A.S.; Ma, K.; Blaabjerg, F. A Lumped Thermal Model Including Thermal Coupling and Thermal Boundary Conditions for High-Power IGBT Modules. *IEEE Trans. Power Electron.* **2018**, *33*, 2518–2530. [CrossRef]
21. Qin, F.; Zhang, Y.; An, T.; Zhou, R. An Improved Thermal Network Model of Press-Pack IGBT Modules Considering Contact Surface Damage. *IEEE Trans. Device Mater. Reliab.* **2023**, *23*, 444–452. [CrossRef]
22. Zhao, Y.; Wang, Z.; Luo, D.; Chen, C.; Ji, B.; Li, G. Multitimescale Thermal Network Model of Power Devices Based on POD Algorithm. *IEEE Trans. Power Electron.* **2024**, *39*, 3906–3924. [CrossRef]
23. Guo, W.; Ma, M.; Wang, H.; Wang, H.; Song, Q.; Chen, W. A Partition Decoupling Algorithm for Compact Thermal Model in Multichip IGBT Modules. *IEEE Trans. Power Electron.* **2023**, *38*, 66–72. [CrossRef]
24. Wang, Z.; Qiao, W. A Physics-Based Improved Cauer-Type Thermal Equivalent Circuit for IGBT Modules. *IEEE Trans. Power Electron.* **2016**, *31*, 6781–6786. [CrossRef]
25. Du, M.; Guo, Q.; Wang, H.; Ouyang, Z.; Wei, K. An Improved Cauer Model of IGBT Module: Inclusive Void Fraction in Solder Layer. *IEEE Trans. Compon. Packag. Manuf. Technol.* **2020**, *10*, 1401–1410. [CrossRef]
26. Hu, Z.; Zhou, Y.; Zhang, T.; Jiang, Y. An Adaptive Electrothermal Model for Estimating the Junction Temperature of Power Device. *IEEE Trans. Electron Devices* **2021**, *68*, 3475–3482. [CrossRef]
27. Eleffendi, M.A.; Johnson, C.M. Application of Kalman Filter to Estimate Junction Temperature in IGBT Power Modules. *IEEE Trans. Power Electron.* **2016**, *31*, 1576–1587. [CrossRef]
28. Li, R.-R.; Zhang, Y.-H.; Wang, Y.-F.; Wang, L.-B. Convective Heat-Transfer Characteristics of a Channel with One Surface Having Mini-Grooves in the Flow Direction and a Plain Surface Located at a Mini-Distance. *IEEE Trans. Compon. Packag. Manuf. Technol.* **2015**, *5*, 65–74. [CrossRef]
29. Han, J.; Liu, K.; Gao, Y.; Yan, P. Transient Thermal Design for Inverter Unit of High-Voltage Capacitor Charging Power Supply. *IEEE Trans. Plasma Sci.* **2017**, *45*, 1651–1655. [CrossRef]
30. Heng, K.; Yang, X.; Wu, X.; Ye, J. A 3-D Thermal Network Model for Monitoring of IGBT Modules. *IEEE Trans. Electron Devices* **2023**, *70*, 653–661. [CrossRef]
31. Yu, D.; Liao, X.; Wang, Y. Modeling and Analysis of Caputo–Fabrizio Definition-Based Fractional-Order Boost Converter with Inductive Loads. *Fractal Fract.* **2024**, *8*, 81. [CrossRef]
32. Wang, Z.-B.; Liu, D.-Y.; Boutat, D.; Zhang, X.; Shi, P. Nonasymptotic Fractional Derivative Estimation of the Pseudo-State for a Class of Fractional-Order Partial Unknown Nonlinear Systems. *IEEE Trans. Cybern.* **2023**, *53*, 7392–7405. [CrossRef] [PubMed]
33. Almatroud, O.A.; Khennaoui, A.-A.; Ouannas, A.; Alshammari, S.; Albosaily, S. A New Fractional Discrete Memristive Map with Variable Order and Hidden Dynamics. *Fractal Fract.* **2024**, *8*, 322. [CrossRef]
34. Baishemirov, Z.; Berdyshev, A.; Baigereyev, D.; Boranbek, K. Efficient Numerical Implementation of the Time-Fractional Stochastic Stokes–Darcy Model. *Fractal Fract.* **2024**, *8*, 476. [CrossRef]
35. Barbero, G.; Evangelista, L.R.; Zola, R.S.; Lenzi, E.K.; Scarfone, A.M. A Brief Review of Fractional Calculus as a Tool for Applications in Physics: Adsorption Phenomena and Electrical Impedance in Complex Fluids. *Fractal Fract.* **2024**, *8*, 369. [CrossRef]
36. Sarfraz, M.; Zhou, J.; Ali, F. An 8D Hyperchaotic System of Fractional-Order Systems Using the Memory Effect of Grünwald–Letnikov Derivatives. *Fractal Fract.* **2024**, *8*, 530. [CrossRef]
37. Coello, C.A.C.; Pulido, G.T.; Lechuga, M.S. Handling multiple objectives with particle swarm optimization. *IEEE Trans. Evol. Comput.* **2004**, *8*, 256–279. [CrossRef]

38. You, W.-B.; Ding, Y.-H. W-MOPSO in Adaptive Circuits for Blast Wave Measurements. *IEEE Sens. J.* **2021**, *21*, 9323–9332. [CrossRef]
39. Ravelo, B.; Agnus, B.; Carras, S.; Davin, T. Cauer Ladder Inspired Kron–Branin Modeling of Thermal 1-D Diffusion. *IEEE Trans. Circuits Syst. II Express Briefs* **2020**, *67*, 27–31. [CrossRef]

Disclaimer/Publisher's Note: The statements, opinions and data contained in all publications are solely those of the individual author(s) and contributor(s) and not of MDPI and/or the editor(s). MDPI and/or the editor(s) disclaim responsibility for any injury to people or property resulting from any ideas, methods, instructions or products referred to in the content.